Mineralogical Analysis of Solid Sample Flame Emission Spectra by Machine Learning

Adam Bernicky[1], Boyd Davis[2], Milen Kadiyski[3], Hans-Peter Loock[4]*

1 Queen's University, Department of Chemistry, 90 Bader Lane, Kingston, ON, Canada

2 Kingston Process Metallurgy Inc., 759 Progress Avenue, Kingston, ON, Canada

3 Aurubis Bulgaria, Industrial Zone, 2070 Pirdop, Bulgaria

4 University of Victoria, Department of Chemistry, 3800 Finnerty St., Victoria, BC, Canada

ABSTRACT: Solid pre-concentrated ore samples used in pyrometallurgical copper smelters are analysed by flame emission spectroscopy using a specialized flame OES system. Over 8500 complex spectra are categorized using an artificial neural network, ANN, that was optimized to have ten hidden layers with 40 nodes per layer. The ANN was able to quantify the elemental content of all samples to within better than 1.5% w/w, and was able to identify the prevalent minerals to within better than 2.5%w/w. The flame temperature was obtained with an uncertainty of 3 K and the particle sizes to within 2 μm. The results are found to be superior to those obtained to a non-linear partial least squares fit model, which is equivalent to an ANN having no hidden layers.

INTRODUCTION

Flash Smelting is a common pyrometallurgical process which is used worldwide to extract base metals, such as copper, iron, or zinc, from finely pulverized mineral ores. For example, copper flash furnace smelting produces enriched copper matte (sulphide) with an estimated copper concentration of up to 75%.[1] For these processes, it is difficult to implement observational systems to provide meaningful feedback to process operators. Despite the large throughputs of industrial flash furnaces (tens to low hundreds of tonnes of concentrate per hour), the process inside the flash furnace is currently not monitored. In addition, physical, chemical and mineralogical information on the feedstock is sparse. The lack of feed-forward process control can frequently produce variable grades in the copper matte product.

Recent work on sensing systems for pyrometallurgical processes has focused on the development of sensors based on fiber optic probes to monitor the flame within the flash furnace.[2-6] The intensity of the flame emission, its temperature from blackbody radiation, and some atomic and molecular information can be obtained from these probes by applying, for example, principal component analysis (PCA) to the spectral datasets.[7] Unfortunately, iron and copper concentrations cannot be quantified from the respective atomic emission lines due to insufficient thermal energy of the flame in a flash furnace. Instead, an ancillary, high-temperate acetylene/nitrous oxide flame generated emission spectra from the same solid samples that showed sufficient information to infer the elemental concentration of the feedstock. A commercial fiber-coupled spectrometer was used to record the spectra and an artificial neural network classified the spectra according to five descriptors, i.e. the concentrations of elements Fe, Cu, Zn, Si and S.[8]

The burner operated without requiring preparation of the samples for its operation, but, in its initial configuration, the flame emission was not stable enough to permit more sophisticated analyses. A new burner that was designed to consume and ionize the pulverized concentrate samples and operate at high temperatures was presented in a companion article.[9]

In this paper, we analyze thousands of spectra obtained with this burner using machine learning. We develop robust and accurate predictive models to determine the chemical, mineralogical, and physical properties of these industrial feedstocks. The development of predictive models allows users to transform quantitative measurements into useful information. This is particularly important in the spectroscopic analysis of complex samples since spectroscopic data can be difficult or impossible to interpret in their raw form.

The most straightforward and familiar models are univariate models where a single measurement is linearly correlated to a single physical descriptor value. For example, a molecular band's absorbance, A, is linearly related to its associated absorption cross-section σ, the molecule's number density, N, and the path length, L, through the Beer-Lambert absorption law. A dilute sample containing different molecules may be analyzed by a decomposition of the measurements weighted by physical descriptors that are characteristic of the molecules (e.g. their product of absorption cross section and number density) with a linearly additive multivariate analysis model.

Unfortunately, this simple model fails as soon as interferences are present, such as inner filter effects, reabsorption, fluorescence, temperature-dependent spectral features, wavelength-dependent scattering, etc. Here, non-linear multivariate models are preferred since interferences can then be modelled and eliminated by combining several measurements.[10] The validity of all predictive models must be rigorously tested to ensure that the models contain, on the one hand, a sufficient level of complex-

ity to describe the studied system but also do not result in overfitting.[11] Predictions made by an underfit model on new data may not provide meaningful descriptor results, whereas overfitting a model reduces its applicability to new data.

Predictive models can be grouped into supervised models and unsupervised models. Unsupervised models are created by applying algorithms to unlabeled datasets in an attempt to fit the dataset with a number of components and an associated score. These scores can be related to physical descriptors, increasing the dataset's interpretability. Principal Component Analysis (PCA) is a widely used multivariate algorithm that explains the variance in a dataset (X) with *n* mutually orthogonal loading vectors.[12] Nonnegative matrix factorization is a related algorithm that best explains variance in a dataset by limiting loading vectors to positive values. A generalized version of PCA known as parallel factor analysis (PARAFAC) is more useful in spectroscopic applications because "neat" spectra associated with each component can be obtained since orthogonal loadings are not required.[13] Frequently, PARAFAC scores can even be related to the relative concentrations of the descriptors.

By contrast, supervised models are created from an algorithm that modifies fitting parameters based on known descriptors obtained independently to minimize the variance of the model. These descriptors can include the concentration or number density of the components, as well as temperature and other physical or chemical properties of the sample. Linear or non-linear regression models like partial least squares (PLS) models decompose measurements by assigning and adjusting weights to all input variables to minimize the variance to the expected output variables, i.e. the descriptors. Artificial neural networks (ANN) also attempt to minimize the variance of the descriptors by adjusting a set of weights and biases that connects the input dataset ("layer"), comprised of predictor data such as spectra, to the output layer, i.e. the set of descriptors. Since ANNs are inherently non-linear regression models that can handle complex non-linear datasets, they are well-suited to complex spectra of a large variety of minerals, such as those present in pyro-metallurgical samples.

EXPERIMENTAL

Five reference mineral samples – Bornite (Cu_5FeS_4), Chalcopyrite ($CuFeS_2$), Pyrite (FeS_2), Pyrrhotite (Fe_7S_8), and Sphalerite, (Zn,Fe)S (all from Grenville Minerals) – were crushed to achieve an approximate particle size of 80-100 µm. In addition, 30 blended samples were prepared from 10 (=4+3+2+1) binary combinations of these five reference samples, each prepared in 25% (w/w) intervals, i.e. at 25:75; 50:50; 75:25 ratios. The other 12 samples were custom mineral concentrates prepared by blending 13 samples provided by an industrial partner (Aurubis, Hamburg, Germany). Elemental and mineralogical analysis was performed on the five reference mineral samples and 12 blended industrial samples.

The concentrations of 5 elements (Cu, Fe, Si, Zn, Ni) were determined by Inductively-coupled Plasma – Optical Emission Spectroscopy, ICP-OES, by the sodium peroxide fusion method. Sodium hydroxide and sodium peroxide with 0.2 g of sample were heated in an oven at 550ºC and then digested with concentrated hydrochloric acid at elevated temperatures on a hot plate. The sample was then cooled and diluted before performing ICP-OES analysis. Sulphur was quantified by combustion using infrared spectroscopic quantification of SO_2 (ELTRA - CS2000). The elemental analysis accounted for between 70-99% of the total mass of the samples listed in Table S1 of the Supplementary Information. The remainder can be attributed to oxygen-bearing minerals, as discussed in the following section.

Mineral Liberation Analysis, MLA

Each sample was embedded in epoxy resin, which was then ground down and polished to a near-mirror finish to reveal a representative cross-section of the sample. The polished surfaces were then carbon-coated to prepare them for analysis.

Mineralogical information was obtained by Scanning Electron Microscopy – Energy Dispersive X-ray Spectroscopy (SEM-EDS), which is also known as Mineral Liberation Analysis (MLA). The top row of Figure 1 shows the backscattering electron images obtained by scanning the field of view of the five

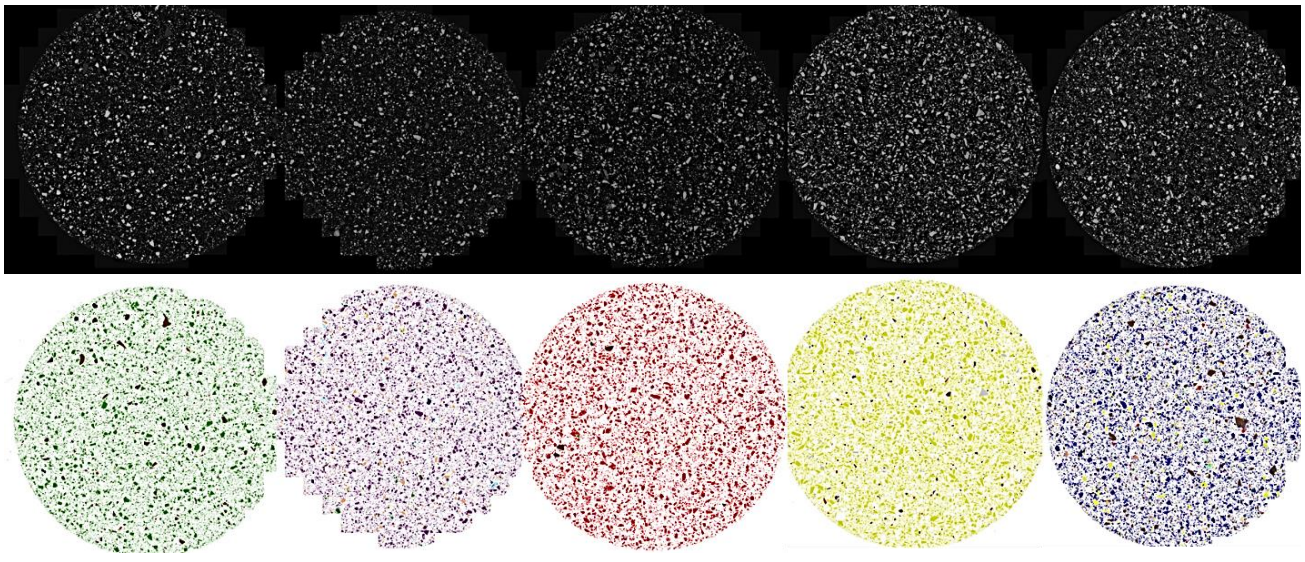

Figure 1. Backscattering electron images (top) and classified (bottom) images of sphalerite, pyrrhotite, pyrite, chalcopyrite, and bornite reference samples (Left to Right).

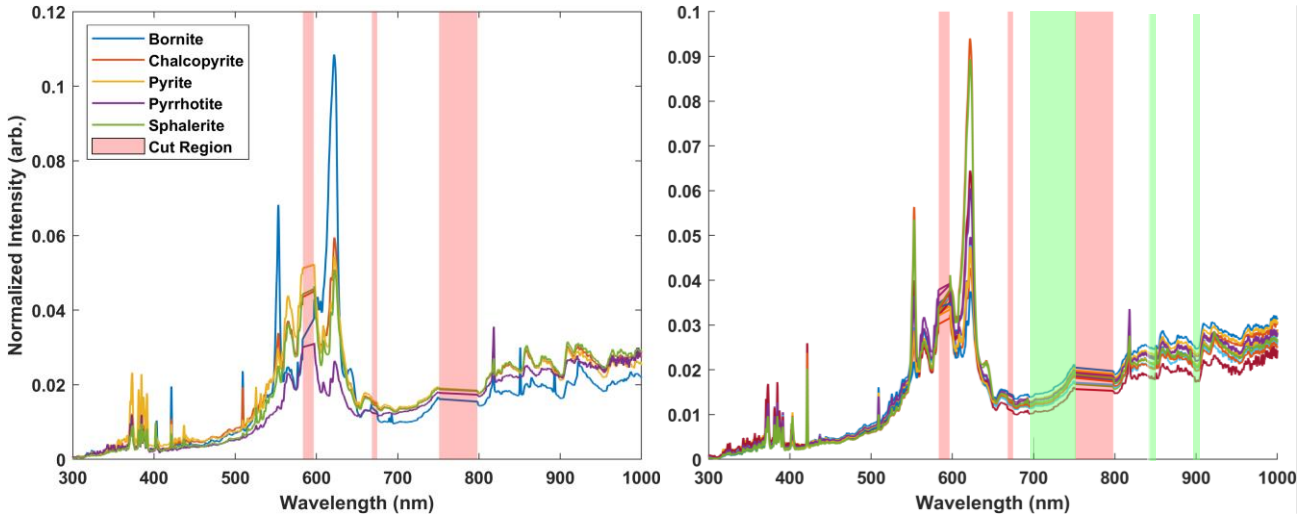

Figure 2. Representative unnormalized emission spectra of reference minerals (left) and 12 concentrate blends (right) obtained from the coaxial burner. Removed regions are highlighted in red, whereas green regions were used to fit to the black-body equation. The composition of these samples is given in the Supplementary Information Tables S1 and S2.

reference minerals. The grayscale intensity is related to the average atomic number (AAN) of the mineral phase, where a brighter image corresponds to a higher AAN.

Phase segmentation is performed according to AAN and an EDS spectrum is then obtained for each unique mineral phase at its centroid. These EDS spectra are then categorized using a mineral database, and the mineral phase is thereby classified (Figure 1-bottom row). Figure S1 of the Supplementary Material shows the respective classified EDS images for the 12 industrial blends.

After classification, the mass concentration is determined from the total surface area density of each mineral phase. **Table S2** of the Supplementary Information captures the results of the SEM-EDS mineralogical analysis by listing the concentrations of the 12 most abundant minerals.

In all cases, the major mineral phase for the reference mineral samples was determined as expected, with the chalcopyrite sample having the highest purity. Bornite and Pyrite samples contain nearly 15% chalcopyrite and pyrrhotite, respectively, which is not unexpected given the respective chemical similarities. Sphalerite exhibited a mixture of sphalerite, ZnS, and iron-included sphalerite, $(Zn_x,Fe_{1-x})S$. Oxygen-bearing minerals such as dolomite, fayalite, hornblende, magnetite, and quartz are the cause of the unaccounted-for mass from ICP analysis.

Particle Size Analysis by MLA

The particle size distribution of the sample was obtained following the MLA classification of the mineral phases. In a separate study, we observed that particle size strongly determined the desulfurization of concentrates, with smaller particles more likely to be fully desulfurized in the flame.[14] A comprehensive model, such as the ANN model, must be able to predict the mean particle size to effectively associate a sample's chemical and physical characteristics.

The particle size distribution was fitted to a piecewise model to determine specific cumulative passing percentages, a common metric in metallurgical feedstock characterization. Five separate particle size metrics are created representing the size of holes through which 50, 60, 70, 80 and 90% of particles pass through. The corresponding average particle sizes are 35±10 μm, 44±12 μm, 55±15 μm, 70±21 μm, and 93±27 μm.

Data Acquisition and Preparation

Each sample was analyzed using the flame emission sensor system that was designed for the direct analysis of heterogeneous feed materials as described previously.[9] Briefly, the flame emission system is based on an acetylene:nitrous oxide burner consisting of eight angled holes arranged on a ring through which the premixed fuel:oxidant mixture is directed towards the centre of the flame. This ring of burner nozzles is arranged around a larger open hole through which the pulverized solid sample is fed by gravity. Upstream of the burner plate, the solid sample is drawn into the carrier air stream using a Venturi nozzle. The

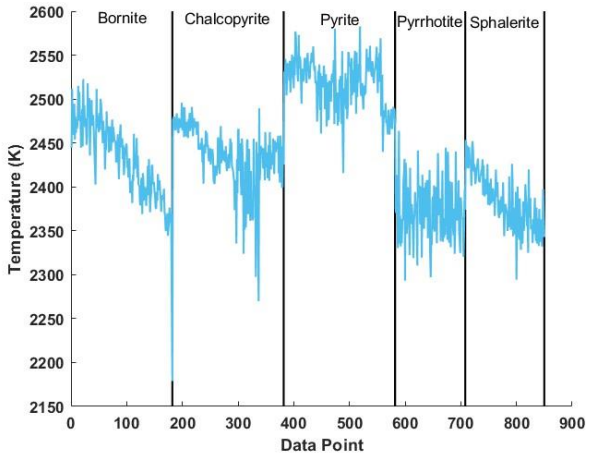

Figure 3. A comparison of the flame temperature for reference mineral samples obtained from fitting response-corrected emission spectra (see Figure S2 in the supplementary material).

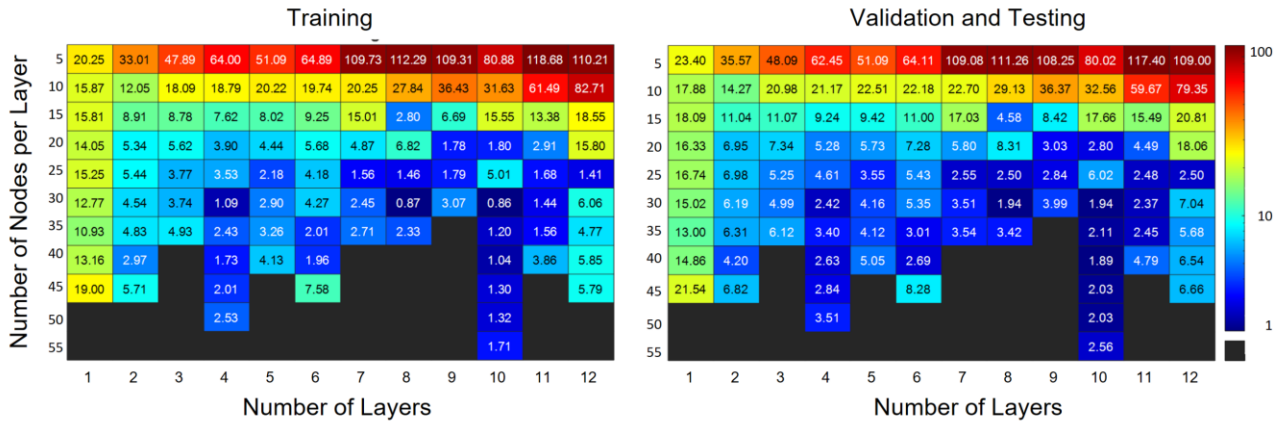

Figure 4. RMSE obtained by altering the total number of nodes (rows) found in the hidden layers and the number of hidden layers (columns) for the training set and the testing and validation set (bottom). Colour scaling is represented logarithmically.

burner and flame are contained in a vessel to direct combustion products into the exhaust. The emission from the flame is monitored using a spectrometer that is coupled to the chamber using an armored fiber-optic cable.

The spectrometer records 100 spectra per second. We average ten of these spectra for a data acquisition rate of ten averaged spectra per second. For each of the 47 samples, 250 averaged spectra were recorded, thereby producing 11,750 spectra in total. Spectra that are saturated or too low in intensity were discarded, resulting in 8561 unique emission spectra that met preprocessing requirements. These spectra each contain measurements at 2480 wavelengths between 300 nm and 1000 nm, with an average spectral resolution of 0.6 nm.[15] Representative spectra for each pure reference sample and blended industrial samples are displayed in **Figure 2**.

The presence of alkali metals usually produces saturated emission lines that are not useful in predictive models since their intensity is not related to the samples' composition. These emission lines are associated with sodium (589.0 and 598.6 nm), lithium (670.8 nm), and potassium (766.5 and 769.9 nm). Therefore, these wavelength regions were removed from the spectrum. Cut regions are shown in pink in **Figure 2**.

Results and Discussion

Flame temperature

The flame temperature associated with the emission spectrum of each sample was obtained using a fit of the black body spectrum to sections of the spectrum. A correction factor accounting for the spectrometer's response function was obtained following calibration with a calibrated black body emitter.[9] Several sections of the spectrum which contained little or no atomic and molecular emission features were selected to fit the black body emission equation.[9] As anticipated, the average blackbody temperature of 2400 ± 70 K for the nitrous oxide:acetylene flame is nearly 200 K lower compared to oxy-acetylene flames.[8,12]

Figure 3 indicates that some solid feeds can reduce the flame's temperature more than others. The thermal properties of these sample mixtures, such as enthalpy of combustion (ΔH_{comb}) and enthalpy of heating (ΔH_{heat}) influence the flame temperature. Bornite and Sphalerite, having the highest silica content, decrease the flame temperature, while Pyrite, FeS_2, and Pyrrhotite, Fe_7S_8, maintain the flame temperature. The flame temperature difference between Pyrite and Pyrrhotite may appear large, considering their similar elemental composition. However, the colder burning Pyrrhotite contains only about half as much sulphur, reducing the enthalpy of combustion. It also contains over 8% of dolomite, $CaMg(CO_3)_2$.

ANN Analysis of elemental and mineralogical composition

A custom code was written in the MATLAB™ environment using the *Statistics and Machine Learning Toolbox* to randomly divide each of the two spectral data sets, i.e. those obtained by recording flame emission spectra for the five reference minerals and for the 12 blends, into training, testing, and validation subsets in a ratio specified by the user. The training algorithm is a scaled gradient descent algorithm that uses the performance gradient of the training subset to optimize the model while being monitored by the performance of a separate validation subset.[16] A descriptor label is assigned to each measurement (i.e. spectrum) based on externally validated properties.

To determine the required size and complexity of the ANN architecture, our code starts by training a network without a hidden layer ($k = 0$). This corresponds to a baseline performance of the simplest ANN having a given number of input nodes, n_0, and output nodes, n_{out}. Here, n_0 corresponds to the 2272 intensity measurements at $n_0 = 2272$ different wavelengths (2480 wavelength channels minus the cut regions), and $n_{out} = 24$ corresponds to 6 element concentrations, 12 mineral concentrations, five particle size ranges and the flame temperature. The convergence criterion held to 5 validation failures to ensure proper model generalization. The code then increases the complexity of the model by one hidden layer. We then increase the number of nodes, n, in this hidden layer until a stopping criterion is met. The weights and biases of each ANN architecture [k, n] are optimized iteratively, and the performance of the testing and validation subsets is determined for each combination of hidden layers, k and nodes, n. This is repeated 30 times with randomly initialized weights and biases to ensure the model's global minimum is reached for a particular architecture [k, n]. The performance trend is calculated to determine if a global minimum has been reached and to prevent unnecessary training.

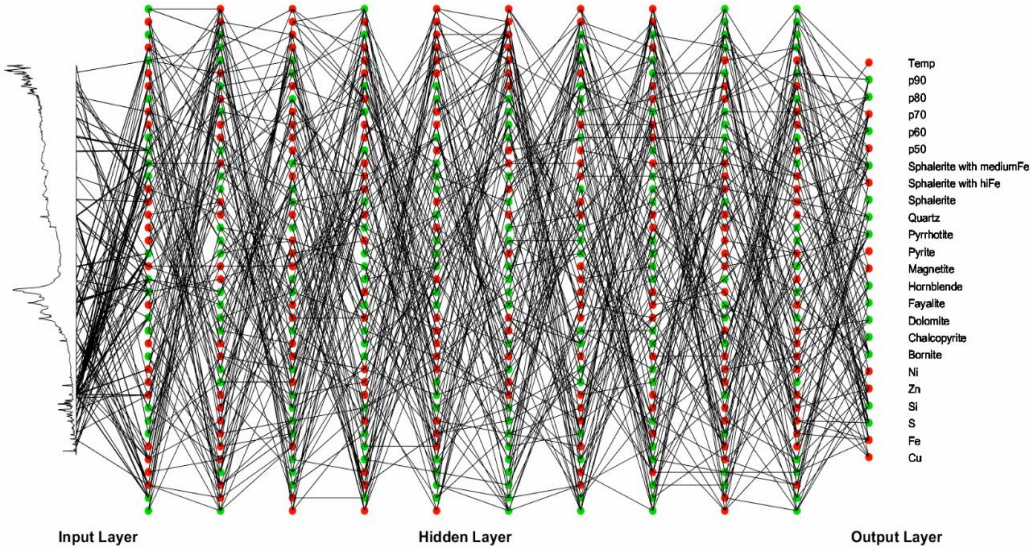

Figure 5. An illustration of the best combined ANN produced from the training algorithm by drawing the connections with the strongest magnitude. The weight of connections between the input layer and the first hidden layer is represented by the thickness of the line. The three strongest connections to the next layer are displayed with uniform line thickness for all other layers.

Specifically, the performance of each new ANN architecture is compared to the two previous ANN architectures [*k*, *n-1*] and [*k*, *n-2*]. If the current ANN architecture performs worse than the previous two ANN architectures, the model stops increasing the number of nodes and instead increases the number of hidden layers by one; the process is then repeated.

Figure 4 shows the best performance of the training and validation/testing subsets for each architecture, where the root mean square error, RMSE, was used as the performance metric.

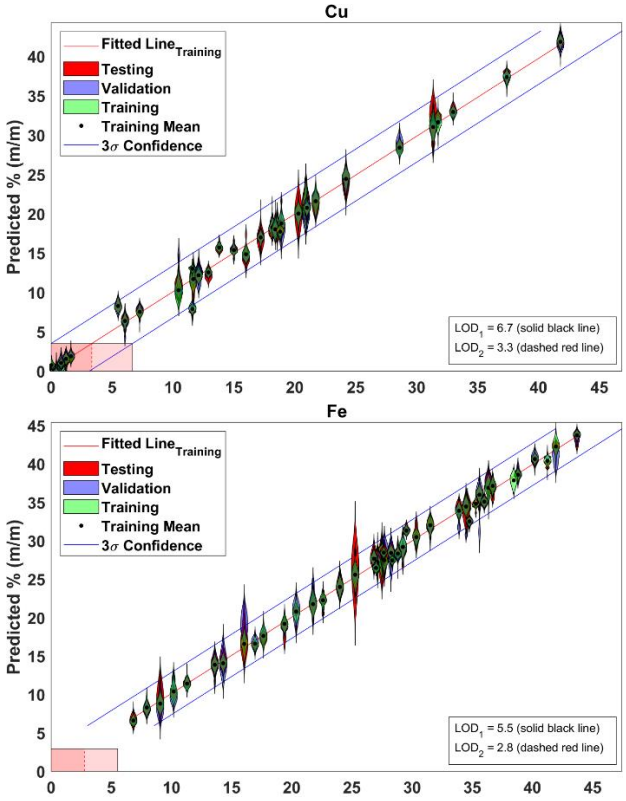

Figure 7. Violin correlation plots for elemental descriptors with a distribution of ANN model error and LOD for 2-norm normalization dataset. Blue lines depict 99% confidence intervals.

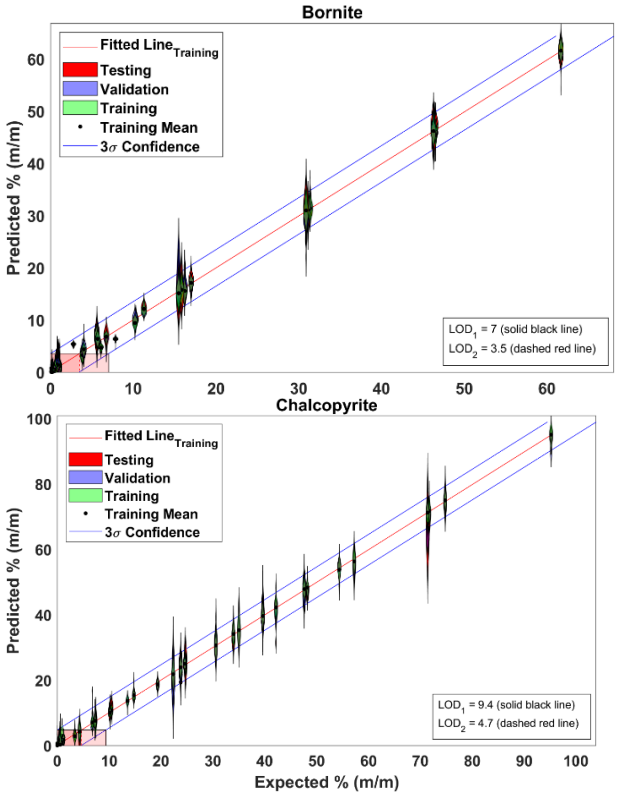

Figure 6. Violin correlation plots for mineral descriptors with a distribution of ANN model error and LOD for 2-norm normalization dataset. Blue lines depict 99% confidence intervals.

We obtain performance characteristics of ANN architectures with an increasing number of hidden layers where each architecture has an identified optimal number of nodes. Should two models with different architectures produce similar performance, the model with fewer total nodes is selected because the number of weighted connections is given by $n(n_0 + n_{out}) + (k-1)n^2$ when $k \geq 1$ and the cost of the calculation increases accordingly.

In our case, the ANN required approximately 130 hours of training before the algorithm converged, i.e. increasing the number of nodes and hidden layers no longer improved the performance. The ANN architecture that produces both the best validation and testing performance minima is found for the ANN with ten hidden layers and 30-40 nodes per layer (**Figure 4**, Figure 5).

As will be discussed below, the prediction uncertainty of the validation and testing subsets for elemental and mineralogical composition is ~1%, whereas the particle size can be determined with an uncertainty of 3 μm and the temperature within ~6 K. We also found that the non-linear predictive ANN model improves the accuracy of the compositional descriptors over linear PLS models.

The predictive capabilities of the combined ANN model for the elemental descriptors and major mineral descriptors are illustrated using vertical correlation plots in Figure 6 and Figure 7, respectively. The expected and predicted values for major elements (Cu, Fe, S, Zn) exhibit excellent correlation (r^2>0.98) and a normal error distribution – see also Figure S2 in the Supplementary Information. The limit of detection, LOD, was calculated from the 99% (3σ) confidence intervals represented with blue vertical lines in Figure 6 and Figure 7. The correlation between expected and predicted concentrations for the minor elements (Si, Ni) is comparably low, resulting in an LOD that is comparable to the predicted concentrations obtained for these descriptors. (Figure S2)

Turning to the mineralogical identification, the major mineral species, such as bornite and chalcopyrite, show good correlation and low relative LOD, while the minor species, like silica, are determined with a LOD that is too large for most predictions (Figure 7 and Figure S3 in the supplementary information). Indeed, we can see from Table 1 that LOD_1 is similar in absolute concentrations for all minor constituents. This is a consequence of a combined descriptor fit and using a common RMSE as a performance metric to train the predictive models.

The above analysis draws the testing set from the same pool of spectra as the training and validation sets. Therefore, this procedure does not apply the model to mixtures of minerals on which it had not been trained. In essence, until now, we have only tested whether the model can recognize the spectra on which it had been trained. A more meaningful analysis is a test by which a *new* blend of minerals is introduced at the testing stage, or, equivalently, to remove one of the blends from the training and validation sets and only introduce it at the testing stage.

Blend #7 was removed from the dataset prior to training the network. The resulting ANN training and validation subset achieved an average RMSE of 2.2%, while Blend #7 produced a RMSE of 2.5%. Figure 8 shows that the model continues to produce an excellent correlation between the expected values (from independent measurements) and the predicted values by the model.

Finally, we tested how well a simple non-linear Partial Least Squares fit, PLS, would model the data sets. We removed all hidden layers and performed an ANN optimization that connected the input and output layers through non-linear activation functions. The resulting RMSE values are listed in **Table 1** and show a PLS performance that is worse by at least a factor of two in nearly all descriptors compared to the optimized ANN model.

Of course, any linear correlation (not shown) between two patterns from predictor fingerprints and descriptor values is ultimately based on a linear addition or subtraction of spectra, i.e. it implies that each mineral contributes a unique spectrum to the experimental predictor spectrum. We expect linear models to perform even worse than the more flexible non-linear PLS. Non-linear modelling addresses some of the shortcomings associated with linear PLS, but only the ANN is able to address the effects of reabsorption, scattering, temperature, or particle size corrections effectively.

Determination of the Limit of Detection, LOD

In the above analysis, the limit of detection (LOD) was determined from the linear correlation curve, according to Loock and Wentzell.[17] The more commonly used LOD_2 assumes an error-free regression of expected and model prediction where the sensitivity (s) and the uncertainty of the model of prediction (σ_y) are obtained from a linear regression.

$$x_{LOD2} = \frac{t\sigma_y}{s} \tag{1}$$

A confidence interval of 99% was determined by setting the student t-function value to $t = 3$. A more meaningful second value, LOD_1, was calculated by determining the uncertainty of fitted parameters and propagating the error.[17] The formula accounts for the number of replicates (k) and data points (n).

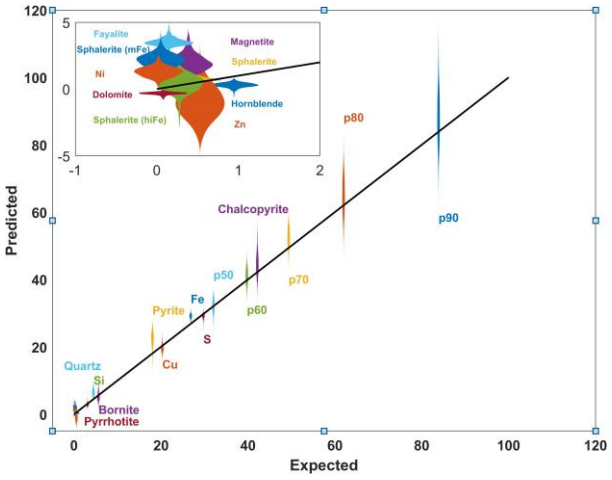

Figure 8. A violin correlation plot of multiple descriptors constructed from the output of the Leave-One-Out ANN model

***Table 1**: RMSE in mass% (except where indicated) of PLS and ANN predictive models on data subsets after training. The calculated LOD is also included from the ANN model.*

	PLS		*ANN*			
Descriptor	**Training**	**Validation**	**Training**	**Validation**	**Testing**	**LOD_1**
Cu	1.64	1.94	0.77	0.98	0.95	6.7
Fe	1.94	2.29	0.59	0.91	0.93	5.5
S	1.96	2.43	0.67	0.83	0.89	5.4
Si	0.63	0.76	0.50	0.56	0.53	6.8
Zn	2.55	3.13	0.69	1.27	1.28	5.8
Ni	0.43	0.50	0.59	0.63	0.63	7.5
Bornite, Cu_5FeS_4	2.69	3.21	0.87	1.17	1.24	7.0
Chalcopyrite, $CuFeS_2$	4.93	6.15	1.11	1.64	1.58	9.4
Dolomite, $CaMg(CO_3)_2$	0.32	0.36	0.23	0.25	0.25	2.2
Fayalite, Fe_2SiO_4	1.20	1.43	0.54	0.54	0.59	4.1
Hornblende, $Ca_2(Mg,Fe,Al)_5(Al,Si)_8O_{22}(OH)_2$	0.67	0.79	0.47	0.51	0.50	5.8
Magnetite, Fe_3O_4	0.67	0.79	0.31	0.33	0.31	5.6
Pyrite, FeS_2	4.76	5.86	1.09	1.88	2.09	8.8
Pyrrhotite, Fe_7S_8	2.67	3.05	0.94	1.35	1.39	7.0
Quartz, SiO_2	1.33	1.58	0.97	1.03	1.00	7.5
Sphalerite, (Zn,Fe)S	0.56	0.69	0.46	0.56	0.54	3.6
Sphalerite (hiFe)	3.14	3.85	0.83	1.56	1.55	6.8
Sphalerite (medFe)	0.47	0.58	0.31	0.36	0.38	2.4
p50 /micron	2.16	2.83	0.63	0.82	0.77	5.2
p60 /micron	2.61	3.42	0.54	0.77	0.71	4.7
p70 /micron	3.17	4.13	0.59	0.85	0.84	5.0
p80 /micron	4.18	5.39	0.62	0.92	0.98	5.6
p90 /micron	5.44	6.96	0.80	1.19	1.26	7.0
Temp /K	6.19	8.17	1.04	2.46	2.43	9.6

$$x_{LOD1} = \frac{2t\sigma_y}{nt^2\sigma_y^2 - Ds^2} \times \left(t\sigma_y \sum_i x_i - \sqrt{\frac{D^2 s^2}{k} + D^2 s^2 \sum_i x_i - n\frac{nDt^2\sigma_y^2}{k} - Dt^2\sigma_y^2} \right) \quad (2)$$

where

$$D = n\sum_i x_i^2 - \left(\sum_i x_i \right)^2 \quad (3)$$

The more suitably defined LOD_1 is shown in Figure 6 and Figure 7 and is given in Table 1.

ANN Training Performance Trends

In Figure 5, a representative image of the ANN has been generated by displaying the strongest weighted connections between the nodes and layers, where we set a threshold to display only the connections with the strongest positive (green dots) and negative (red dot) biases. The weight of the connection between the input layer and the first hidden layer nodes is represented by the line thickness since, here, we can relate the connections to a tangible measurement, i.e., the emission spectrum. For all other interlayer connections, we show only the three strongest connections from each node.

As one might expect, many of the strongest connections between the input and the first hidden layer originate from regions of the spectrum containing atomic/molecular emission information. Interestingly, strong weighted connections are observed in the region of the emission spectrum without atomic or molecular emission features. This is explained by the inclusion of flame temperature as a model descriptor.

In Figure 9, we expand on this analysis and determine the most informative regions of the emission spectra. Here, we select several representative emission spectra from the bornite and pyrite reference minerals and manually increase the intensity at each wavelength. We then observe whether the ANN predicts a consequent positive (green) or negative (red) prediction of the respective descriptor. For example, Figure 9A shows that the spectral regions in which Cu-atomic emission lines are observed are strongly predictive of Cu-concentration. Similarly, wavelength regions associated with Fe and FeO emission lines are strong predictors for Fe concentration (Figure 9B). Input nodes between 1750 nm and 2100 nm are negatively correlated to temperature, whereas input nodes around 1250 nm are positively correlated to the predicted temperature – as one expects from the blue shift of a blackbody emission spectrum with increasing temperature (Figure 9F). Other wavelength regions, such as those associated with molecular bands, strongly influence the temperature descriptor. These responses may be attributed to temperature-dependent population changes and are

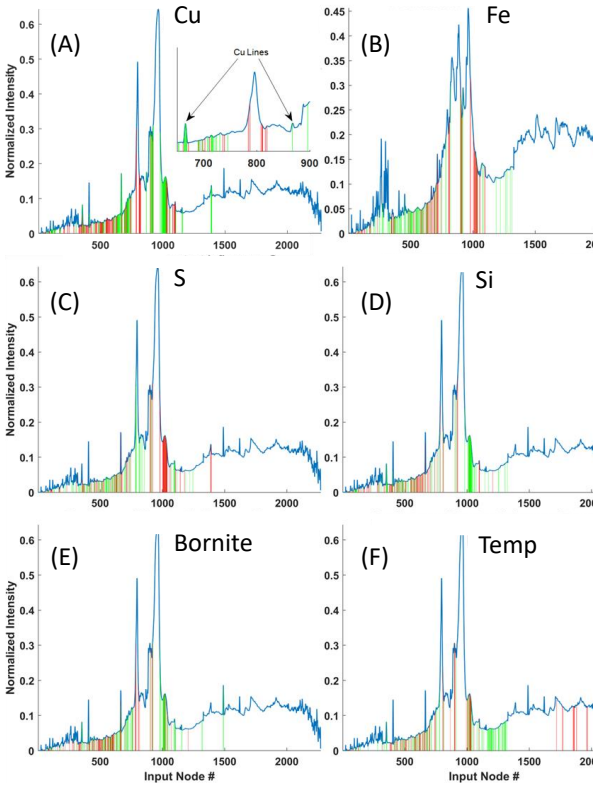

Figure 9. Predictor values in the emission spectrum showing the greatest positive (green) and negative (red) correlation for descriptors Cu, Fe, S, and Si, as well as bornite and temperature. All spectra are from bornite as solid fuel, except (B) which is the pyrite emission spectrum.

governed by the Maxwell-Boltzmann distribution over rovibronic energy levels.

Finally, a heat map of the correlation coefficients, r^2, for all predictor fingerprints is displayed in Figure 10. This correlation plot is rich in information. Firstly, the correlation of temperature to all other descriptors is very low ($r^2 < 0.08$), suggesting the model is able to effectively disentangle the underlying blackbody emission from molecular and atomic signatures contributing to the other descriptors. The correlation diagram points to strong cross-correlations between Ni and Si descriptors as well as between Cu and Fe. As expected, the bornite descriptor, Cu_5FeS_4, is strongly correlated with elemental Cu, Fe, and S, whereas Pyrite, FeS_2, is correlated more strongly with Fe than with Cu. Sphalerite, (Zn,Fe)S, is the only mineral that is strongly correlated to Zn. Also, chalcopyrite is also correlated to Si (and Ni), as expected from its comparably high Si content (Table S1 and Table S2). Correlations to particle sizes indicate that fayalite, hornblende and magnetite are found predominantly in larger particles.

Some compositional descriptors share predictor values, indicating they may share a similar network pathway from input to output nodes. On the other hand, if a pair of descriptor fingerprints exhibited a high correlation, this could also indicate that the model may require the descriptor (intensity at a given wavelength) to have the *opposite* effect, i.e. the strong negative correlation indicates that the ANN effectively differentiate the pair

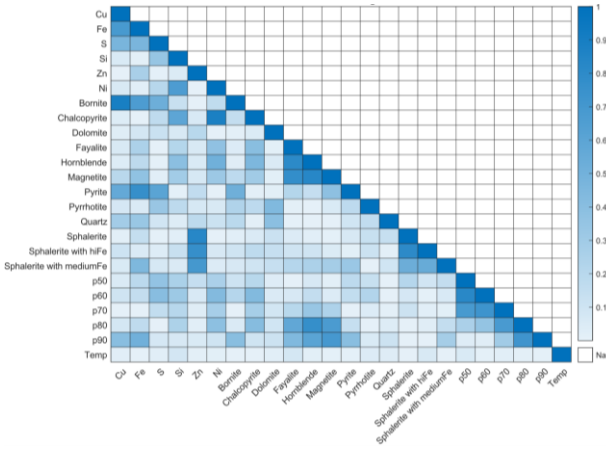

Figure 10. Descriptor correlation, r^2, for all descriptors in the combined ANN.

of descriptors. The predictor fingerprint for bornite and chalcopyrite in Figure 9 illustrates this sharing of predictor values. The copper atomic emission line at 503 nm shows a strong positive correlation with bornite concentration, while we observe a negative correlation for chalcopyrite. Since we know that both bornite and chalcopyrite contain copper, the model has used this predictor variable to differentiate these descriptors.

CONCLUSIONS

The analysis of 47 concentrated metal sulphide powders consisting of reference minerals, their mixtures and industrial mineral samples using a novel solid-phase flame-emission spectrometer produced a large spectral dataset of over 8500 spectra with intensity measurements at 2272 wavelengths/spectrum. Before applying iterative PLS and ANN training algorithms, the emission dataset was labelled with independently obtained descriptors for elemental and mineralogical composition, particle size, and temperature.

The prediction of the concentrations using the ANN was much more reliable compared to non-linear PLS models and allowed us to model concentrations of critical minerals to within a better than 2% percent of their actual values. The flame temperature was predicted by the same ANN with a temperature of better than 3 K, and the average particle size was given with a precision of better than 2 μm. The ANN was also able to predict the composition of mixtures when they were not part of the training and validation sets. The root-mean-squared errors on left-out data were higher by about 30% and accurate within 2.5%, which is more than sufficient for pyrometallurgical process control.

More generally, our analysis indicates that ANNs can play a role in automated analysis and quantification of mineralogical and other samples from spectra that are so complex and numerous that manual analysis would be impossible.

ACKNOWLEDGEMENTS

AB thanks Alain Roy for many useful discussions and Trevor LeBel, Maya Stricker, Chris Pelow, Kathy Golshani, Russell Dawes, and Mark Woodrow for their technical assistance and

advice. HPL and AB are grateful to the Natural Science and Engineering Research Council (NSERC) of Canada for financial support under the Collaborative Research and Development Program. BD thanks the National Research Council of Canada Industrial Research Assistance Program (NRC IRAP) for financial support.

CONFLICT OF INTEREST STATEMENT

BD is the co-founder and Principal of Kingston Process Metallurgy Inc., a company which co-financed the present research.

REFERENCES

1. Group, I. C. S. *World Copper Factbook 2017*; Lisbon, Portugal 2017.
2. Arias, L.; Torres, S.; Toro, C.; Balladares, E.; Parra, R.; Loeza, C.; Villagrán, C.; Coelho, P., Flash Smelting Copper Concentrates Spectral Emission Measurements. **2018,** *18* (7), 2009.
3. Arias, L.; Balladares, E.; Parra, R.; Sbarbaro, D.; Torres, S., Sensors and Process Control in Copper Smelters: A Review of Current Systems and Some Opportunities. **2021,** *11* (1), 1.
4. Myakalwar, A. K.; Sandoval, C.; Sepúlveda, B.; Fuentes, R.; Parra, R.; Balladares, E.; Vásquez, A.; Sbarbaro, D.; Yáñez, J., Laser induced breakdown spectroscopy for monitoring the molten phase desulfurization process of blister copper. *Analytica Chimica Acta* **2021,** *1178*, 338805.
5. Vásquez, A.; Pérez, F.; Roa, M.; Sanhueza, I.; Rojas, H.; Parra, V.; Balladares, E.; Parra, R.; Torres, S., A Radiometric Technique for Monitoring the Desulfurization Process of Blister Copper. **2021,** *21* (3), 842.
6. Yañez, J.; Torres, S.; Sbarbaro, D.; Parra, R.; Saavedra, C., Analytical instrumentation for copper pyrometallurgy: challenges and opportunities. *IFAC-PapersOnLine* **2018,** *51* (21), 251-256.
7. Stokreef, A. Measuring the Effect of Concentrate Mineralogy on Flash Furnace Smelting Using Drop Tower Testing and a Novel Optical Probe. Queen's University, 2018.
8. Bernicky, A.; Davis, B.; Barnes, J.; Loock, H. P., Spectroscopic characterisation of feedstock for copper smelters by machine-learning. *Canadian Metallurgical Quarterly* **2023**.
9. Adam Bernicky, B. D., Hans-Peter Loock, Burner system for solid sample flame emission spectroscopy. 2024.
10. Næs, T.; Martens, H., Multivariate calibration. II. Chemometric methods. *TrAC Trends in Analytical Chemistry* **1984,** *3* (10), 266-271.
11. Hawkins, D. M., The Problem of Overfitting. *Journal of Chemical Information and Computer Sciences* **2004,** *44* (1), 1-12.
12. Bro, R.; Smilde, A. K., Principal component analysis. *Analytical Methods* **2014,** *6* (9), 2812-2831.
13. Bro, R., PARAFAC. Tutorial and applications. *Chemometrics and Intelligent Laboratory Systems* **1997,** *38* (2), 149-171.
14. Dunn, J. G., The oxidation of sulphide minerals. *Thermochimica Acta* **1997,** *300* (1), 127-139.
15. Avantes, AvaSpec-ULS2048x64-EVO SensLine High UV and NIR Sensitivity Spectrometer. **2024**.
16. Xu, Y.; Goodacre, R., On Splitting Training and Validation Set: A Comparative Study of Cross-Validation, Bootstrap and Systematic Sampling for Estimating the Generalization Performance of Supervised Learning. *Journal of analysis and testing* **2018,** *2* (3), 249-262.
17. Loock, H.-P.; Wentzell, P. D., Detection limits of chemical sensors: Applications and misapplications. *Sensors and Actuators B: Chemical* **2012,** *173*, 157-163.